



**HAL**  
open science

## Self-running bearing diagnosis based on scalar indicator using fast order frequency spectral coherence

Souhayb Kass, Amani Raad, Jérôme Antoni

### ► To cite this version:

Souhayb Kass, Amani Raad, Jérôme Antoni. Self-running bearing diagnosis based on scalar indicator using fast order frequency spectral coherence. *Measurement*, 2019, 138, pp.467-484. 10.1016/j.measurement.2019.02.046 . hal-02483683

**HAL Id: hal-02483683**

**<https://hal.science/hal-02483683>**

Submitted on 22 Oct 2021

**HAL** is a multi-disciplinary open access archive for the deposit and dissemination of scientific research documents, whether they are published or not. The documents may come from teaching and research institutions in France or abroad, or from public or private research centers.

L'archive ouverte pluridisciplinaire **HAL**, est destinée au dépôt et à la diffusion de documents scientifiques de niveau recherche, publiés ou non, émanant des établissements d'enseignement et de recherche français ou étrangers, des laboratoires publics ou privés.



Distributed under a Creative Commons Attribution - NonCommercial 4.0 International License

## Self-Running Bearing Diagnosis Based on Scalar Indicator using Fast Order Frequency Spectral Coherence

**Corresponding Author:** Mr. souhayb kass,

**Corresponding Author's Institution:** Lebanese University, Beirut, Lebanon  
and Laboratoire Vibrations Acoustique, Univ Lyon, INSA-Lyon, LVA EA677,

F-69621 Villeurbanne, France

**First Author:** souhayb kass

### Abstract

In vibration-based diagnosis of rolling element bearings, the complexity of the signals requires an expert to use advanced signal processing tools and to interpret the results based on his/her experience. Recently, a few autonomous methods have been proposed to alleviate the demand on the user's expertise, yet they have been mainly focused on fault detection. This paper follows a similar direction but with wider objectives: it aims to develop an indicator that is able to detect, identify and classify typical faults on rolling elements, inner and outer-race. The indicator is based on the recently developed Fast Order-Frequency Spectral Coherence, a key tool of the theory of second-order cyclostationary processes: it condenses the whole information initially displayed in three dimensions into a scalar and provides an interpretation in terms of a probability of presence of a fault. In addition, the proposed indicator is able to return information for different levels of damages in both stationary and non-stationary operating conditions. It takes into consideration uncertainties in the bearing characteristic frequencies, which is crucial in bearing diagnosis. A new pre-processing step is provided to ensure an efficient and constant statistical threshold. The proposed indicator is intended to be used in an autonomous process without the need for visual analysis and human interpretation. The proposed indicator is compared with a recent indicator based on the Envelop Spectrum, in terms of classification and detection performance. Several applications using real and simulated data eventually illustrate the capability for self-running diagnosis.

*Keywords:* Scalar indicator, Probability of presence of a fault, Fast Order-Frequency Spectral Correlation.

### 1 Introduction

Rotating machinery is the major component of an industrial environment. In turn, rolling element bearings (REB) are among the most crucial elements in rotating machinery [1]–[3]. They are designed to reduce the shaft rotational friction for transferring loads to stationary housings and for supporting radial and axial loads. REB failure is one of the most common problems that occur with a high probability [4], up to 90% in small machines [5]. Its corresponding faults, such as rolling element, inner and outer-race faults, should be diagnosed at an early stage to minimize the repair time and to avoid equipment and personnel potential damage.

Many monitoring techniques depend on the visual human ability to identify the presence of faults. In the last two decades, some autonomous methods have been developed to reduce the reliance on human intervention. Since it has been reported that the majority of mechanical failures are preceded by noticeable clues [6], several studies have been published on the use of vibration and acoustic-based indicators for the detection and diagnosis of bearing fault [6]–[8].

These methods can be classified into three categories based on indicators with one, two and three-dimensions, respectively. The one-dimensional methods are based mainly on the computation of the root-mean-square, the crest factor and the kurtosis [9], [10]. Unfortunately, those indicators are essentially confined to the detection of potential abnormalities but cannot identify a specific fault. Two-dimensional methods such as the spectrum, the cepstrum, and

the envelope spectrum (ES) [11]–[13] are based on transforming the signal to the frequency domain or other auxiliary domain. Their advantage over time-domain analysis is their ability to identify and isolate certain frequency components of interest, yet their interpretation is often visual. Examples of three-dimensional methods are the spectrogram [14], the scalogram and the Wigner-Ville distribution [15], which aim at displaying a signal in both the time and the frequency domains. They usually suffer from a high demand on the user expertise for both their application and in their interpretation.

Beside the above classical methods, the diagnosis of REB has been significantly improved in the last decades thanks to the theory of cyclostationary processes. Vibration signals from REB exhibit high levels of cyclostationarity (CS) – a certain type of nonstationarity characterized by periodic statistics – especially in the presence of localized faults. The exploitation of this property has been proved extremely fruitful to conceive diagnostics tools, with the advantage of allowing synchronization with a given fault frequency [16], [17]. It has been shown that second-order CS (periodicity of the autocorrelation function) is often sufficient to fully detect bearing faults, thus leading to the use of spectral quantities such as the spectral correlation (SC), which is a 3D quantity [18]. Since the 90's, several indicators have been proposed to resume the information contained in the SC signature into a scalar quantity. For instance, the degree of cyclostationarity (DCS) theoretically introduced by Zivanovic and Gardner in Ref. [19] is based on the measurement of a quadratic distance between the cyclostationary and stationary signal spectrum. Some applications dedicated mainly to gear fault detection are found in Refs. [20], [21]. When it comes to bearing diagnosis, DCS has shown limitation due to the random slip phenomena [22]–[24], which slightly desynchronizes the fault frequency with respect to its theoretical value. Pennacchi *et al.* [23] tried to overcome this problem by identifying the dependency of the fault frequency deviations on the different operating conditions. Following a different route, Klausen *et al.* [25] proposed a method that is inherently based on a scalar cyclostationary indicator, yet without mentioning the CS framework. Their indicator summarizes the information contained in the envelope spectrum – whose connection with the SC is given in Ref. [12]. Moreover, the interpretation of that indicator may differ from one application to another because of the absence of a predefined threshold. In addition, the calculation of the indicator requires a bandpass filtering step for searching the most suitable frequency band for demodulation, which is achieved without guarantee of optimality. Finally, the method is conceived under the assumption of constant speed with only possibility of slight fluctuations.

The current work aims to remediate drawbacks of the previous methods by providing a scalar indicator that eliminates as much as possible the human intervention in REB diagnosis. The idea is to condensate in a scalar quantity the information provided by the Order-Frequency Spectral Coherence (OFSCoh) proposed in Ref. [26]. The latter is a three-dimensional display of all modulation patterns existing in a signal as a function of the carrier frequency in Hertz and the modulation frequency (also called cyclic frequency) in machine order, which generalizes the SC to nonstationary operations. It is thus considered optimal for revealing bearing fault signatures under stationary and nonstationary speed regimes. The OFSCoh comes with a fast algorithm, the Fast-OFSCoh, which offers new possibilities to quickly compute new indicators. In order to condense its information into a scalar indicator, different steps are followed in the paper. The first one is to integrate the OFSCoh magnitude over the frequency axis, thus leading to an equivalent 2D envelope spectrum. The second step is to standardize the EES in order to force it to have a constant probability distribution with respect to the cyclic order  $\alpha$ . The latter is an original and crucial step as it allows a constant statistical threshold to be set. The third step is to convert the envelope spectrum into a scalar quantity interpreted as a probability of the presence of a fault; this will be achieved through the design of a nonparametric - i.e. without an exact distribution - hypothesis test.

The remaining part of the paper is organized as follows. Section 2 reviews the REB fault signatures and their optimal analysis with the OFSCoh. A non-parametric hypothesis test is introduced in section 3. Section 4 illustrates the use of the hypothesis test for autonomous diagnosis and compares it to a competing method of the literature. Experimental validations

are also made on three benchmark databases in this section. Conclusions and perspectives are given at the end of the paper.

## **2 REB diagnosis exploiting cyclostationarity**

### *2.1 Bearing fault spectral signature*

The expected spectral signatures of REB faults depend on whether the fault is located on a rolling element, the cage, the inner or the outer ring. This allows the expert to easily identify a damage and its location within the bearing components by looking for particular patterns of peaks. The theoretical fault frequencies are calculated in function of the rotational speed and the bearing geometry (the number of rolling elements, contact angle, REB diameter and pitch circle diameter) using well-known formulas (e.g. see Ref [22]).

Although the theoretical fault frequencies are calculated assuming a perfect rolling of the elements, the latter are actually allowed to slip to some extent, which produces a random frequency deviation [22]–[24]. In details, the angle of contact varies with the position of each rolling element, since the ratio of the radial load to the evolution of the axial load changes. Thereby, each rolling element will be located at a different distance from the bearing center and will try to roll at a different speed; while the cage limits the deviation of the rolling elements from their mean position, they are forced to slip [22]. Random frequency deviation, despite being small, compromises the fault follow-up on a frequency basis. Consequently, it implies tracking the fault frequency in a narrow band, typically having a width of a few percent of its central frequency.

The inner-race fault (respectively outer-race and rolling element fault) involves a periodic amplitude modulation characterized by harmonics at the BPOI (respectively BPOO and BSO). Contrary to the outer race fault, the inner-race fault (resp. rolling element fault) has a periodic variation of the transmission path between the fault and the sensor location, which produces side-bands at the shaft frequency  $f_r$  (resp. cage frequency) (Fig. 1). The presence of a radial load has a similar effect.

This section introduces the strategy developed for tracking bearing faults by exploiting their spectral signatures in the OFSC.

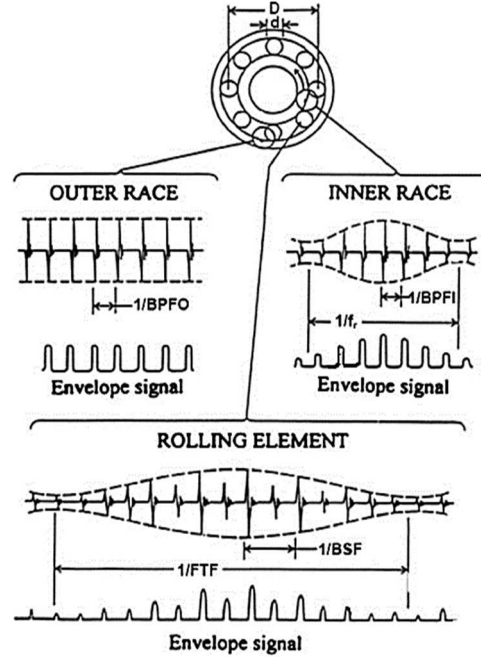


Figure 1. Typical signals and envelope signals from a local REB fault [27].

## 2.2 Bearing Diagnosis using Fast-OFSC

It has been explained in Ref. [28] that classical spectral analysis may fail to detect bearing fault because of masking noise and the marked randomness of the vibrations. Yet, since REB vibrations are cyclostationary, the diagnostic information rises up intact in the cyclic frequency domain in the form of a symptomatic discrete spectral signature. In this work, the Fast-OFSC is used to transform the signal in the cyclic domain. The SC is optimal in the sense that it displays at once, in the form of a bi-spectral map, the whole structure of modulations over the cyclic order  $\alpha$  and of carriers over the classical frequency  $f$  (strictly speaking, it is statistically optimal to describe Gaussian cyclostationary signals, and therefore to design techniques for detection, identification, and possibly quantification of faults endowed with that property). Reference [28] demonstrated the optimality of the SC and its normalized version, the Spectral Coherence (SCoh), not only to evidence the presence of a fault in high levels of background noise but also to return a relative measure of its severity. The Order-Frequency Spectral Correlation (OFSC) is an extension of the SC to account for possible speed variations; it aims at widening the range of applications of classical cyclostationary methods which have been conceived under the assumption of constant speed. Finally, the Fast-OFSC has been recently proposed to reduce the high computational cost of classical estimators of the SC, which may hinder its uses in real-time application.

The Fast-OFSC which considered optimal for revealing bearing fault signatures under stationary and nonstationary speed regimes [26] is used in this paper. This method provides a high-resolution version of the envelope spectrum, from which a scalar indicator will be constructed. Therefore, the authors hypothesize that the indicators developed from the latter will provide a more robust result than that obtained from the envelope spectrum. The mathematical details are given as follows.

First of all, the angle-time autocorrelation function is defined as:

$$R(\theta, \tau) = \mathbb{E}\{x(\theta(t))x(\theta(t - \tau))\}, \quad x(t) \in \mathbb{R} \quad (1)$$

where  $\theta(t)$  is the angle of rotation (in radian) of the reference shaft at time  $t$  and symbol  $\mathbb{E}$  denotes the ensemble average. Next, the OFSC  $S_X^{OF}(\alpha, f)$  is defined as the double Fourier transform of the  $R(\theta, \tau)$ ,

$$S_X^{AF}(\theta, f) = \mathcal{F}_{\tau \rightarrow f}\{R_X(\theta, \tau)\} \quad (2)$$

$$S_X^{OF}(\alpha, f) = \lim_{\theta \rightarrow \infty} \frac{1}{\theta} \int_{\theta} S_X^{AF}(\theta, f) e^{-j\theta\alpha} d\theta = \lim_{\theta \rightarrow \infty} S_X(\alpha, f; \theta) \quad (3)$$

where, in the first line,  $S_X^{AF}(\theta, f)$  stands for an angle-frequency spectrum (akin to a time-frequency representation) and, in the second line, the limit is taken with respect to the total angular sector  $\theta = \int_{\theta} d\theta = \int_T \dot{\theta}(t) dt$  covered during the recording time  $T$ . The (squared magnitude) OFSCoh is defined by the normalized quantity,

$$\gamma_X^2(\alpha, f) = \lim_{\theta \rightarrow \infty} \frac{|S_X^{OF}(\alpha, f; \theta)|^2}{S_X^{OF}(0, f; \theta) S_X^{OF}(0, f - \alpha; \theta)} \quad (4)$$

Being bounded between 0 and 1, the OFSCoh serves as a useful measure of CS. As explained in Ref. [27], the OFSCoh is interpreted as the OFSC of the whitened signal, which tends to equalize regions with different energy levels and therefore to magnify weak cyclostationary signals. Finally, a high-resolution envelope spectrum – hereafter referred to as the enhanced envelope spectrum (EES)  $I_X(\alpha)$  – is obtained from the integration of the Fast OFSCoh over a given frequency band  $B$ , as follows

$$I_X(\alpha) = \int_B \gamma_X^2(\alpha, f) df \quad (5)$$

In practice, the theoretical OFSC  $S_X^{OF}(\alpha, f)$  is replaced by its estimate  $\hat{S}_X^{OF}(\alpha_k, f_k)$  provided by the Fast-OFSC, from which estimates  $\hat{\gamma}_X(\alpha_k, f_k)$  and  $\hat{I}_X(\alpha_k)$  of the OFSCoh and EES are obtained. When it comes to estimators, it is noteworthy that the axis of the carrier frequency  $f$  and of the modulation frequency  $\alpha$  are discretized as follows:  $f_k = k \Delta f$  and  $\alpha_k = k \Delta \alpha$  where index  $k$  refers to  $k$ -th discrete frequency/order and  $\Delta f$  and  $\Delta \alpha$  are the frequency resolution (in Hz) and the cyclic order resolution (in order), respectively. The integral in Eq. (5) is replaced by discrete sums over the discrete frequencies  $f_k$ . The EES summarizes the information contained in the OFSC; a shown later in the paper, it will serve as the basis to design a scalar indicator used in statistical test.

In order to detect the cyclostationary signature of REB fault, several strategies have been proposed in the literature. Most of them rely on the direct visual inspection of the above quantities in the order-frequency domain  $(\alpha, f)$ . Obviously, the sensitivity of such an approach is rather subjective as it strongly relies on the human expertise. The idea of this paper is to reduce the reliance on human intervention by devising an indicator named ‘‘PPF’’ – which stands for the Probability of Presence of a Fault – rooted on the estimated EES, which summarizes the diagnosis information into a scalar value. Contrary to the derivation of the DCS or of the scalar indicator provided in Ref. [25], a probabilistic approach is followed here; this will provide the indicator with an interpretation in terms of probability of the presence of a fault. The approach is formulated in the next section by means of a hypothesis test.

### 3 Hypothesis testing

#### 3.1 Principle

This section intends to formulate the diagnosis of REB as a statistical hypothesis test to be used in automated diagnosis. The statistical test compares the null hypothesis  $H_0$  against the alternative hypothesis  $H_1$ :

$H_0$ : “The vibration signal does not contain the characteristic fault signature”

$H_1$ : “The vibration signal contains the characteristic fault signature”.

Hypothesis  $H_0$  is rejected in favor of  $H_1$  at the level of significance  $(1 - p)$  if a given “test statistic” (i.e. a quantity derived from the data) exceeds a threshold with a probability of false alarm  $p$ . The challenge is here to design the test statistic of the above hypothesis test, based on the EES of section 2.

Incidentally, a few works have approached the diagnosis of REB from similar statistical tests based on spectral quantities close to those used in the present paper, such as the (classical) envelope spectrum [28], the cyclic polyspectrum [27], the (classical) spectral coherence [29], the Fourier transform of the logarithm of the spectral correlation [30], or the integral of the spectral coherence [28].

In these references, the spectral quantities of interest are usually assumed to follow a chi-square distribution under the null hypothesis test, which holds true asymptotically when  $H_0$  coincides with the assumption of stationarity. In the context of variable regime considered in this paper, many sources of non-stationarity exist even under the null hypothesis. Consequently, the exact distribution of the test statistics is unknown; it is proposed to address it in a nonparametric way (i.e. independently of a specific distribution law) by considering the histogram of the standardized EES  $\hat{I}_X^S(\alpha_k)$ , from which a constant statistical threshold is then returned by the  $100(1-p)\%$  percentile. This is detailed in the next subsection.

### 3.2 The test statistics

The aim of this part is to construct the statistics of the hypothesis test introduced in the previous subsection, based on the estimated EES  $\hat{I}_X(\alpha_k)$  of section 2.2. Under the null hypothesis  $H_0$ , the random field  $\hat{I}_X(\alpha_k)$ , seen as a function of the order variable  $\alpha_k$ , can be shown that have zero probability of being nil at any position  $(\alpha_k)$ . Under the alternative hypothesis  $H_1$ , the difference is that the random field will have higher magnitudes along  $\alpha_p \in \mathcal{B}$ ; where  $\mathcal{B}$  is the union of the bands that contain the P harmonics of interest. The objective is to keep only these values and to zero all the other ones. The following empirical steps are proposed. The first step is to standardize the EES in order to force it to have a constant probability distribution with respect to the cyclic order  $\alpha$ , under the null hypothesis  $H_0$ . In principle, the transformation reads

$$\hat{I}_{eX}^S(\alpha_k) = \frac{\hat{I}_X(\alpha_k) - E\{\hat{I}_X(\alpha_k)|H_0\}}{\sqrt{E\{\hat{I}_X(\alpha_k)^2|H_0\} - E\{\hat{I}_X(\alpha_k)|H_0\}^2}} \quad (6)$$

where  $E\{\dots|H_0\}$  stands for the ensemble averaging operator taken under  $H_0$ . One issue is to replace  $E\{\hat{I}_X(\alpha_k)|H_0\}$  and  $E\{\hat{I}_X(\alpha_k)^2|H_0\}$  in the above equation by estimates obtained from a realization of  $\hat{I}_X(\alpha_k)$  which may either pertain to  $H_0$  or  $H_1$ . Since the difference in  $\hat{I}_X(\alpha_k)$  under the null and alternative hypotheses is essentially marked by the presence of peaks, it is proposed to estimate  $E\{\hat{I}_X(\alpha_k)|H_0\}$  from a running median of  $\hat{I}_X(\alpha_k)$ , say  $\mu_{MED}(\alpha_k)$ , and  $E\{\hat{I}_X(\alpha_k)^2|H_0\}$  from the running median of the absolute deviation, say  $\sigma_{MAD}(\alpha_k)$ . The rationale for using a running median is to leave unaffected informative peaks in the spectral coherence. Therefore, the standardized EES reads

$$\hat{I}_X^S(\alpha_k) = \frac{\hat{I}_X(\alpha_k) - \mu_{MED}(\alpha_k)}{\sigma_{MAD}(\alpha_k)} \quad (7)$$

which returns a “pivotal” statistics (i.e. whose probability distribution does not depend on any unknown parameter). Figure 2 illustrates the process of subtracting the running median (Fig. 2 (b)) and of equalizing by dividing by the running median absolute deviation (c) in order to transform the initial EES  $\hat{I}_X(\alpha_k)$  (Fig. 2 (a)) into its standardized version  $\hat{I}_X^S(\alpha_k)$  (Fig. 2 (d)). It is verified in Fig. 2e that  $\hat{I}_X^S(\alpha_k)$  is distributed around a constant baseline, which represents the expected value of the indicator under  $H_0$ . The presence of a few high peaks is the only difference under  $H_1$ . Therefore, if the fraction of the expected number of peaks in the EES under  $H_1$  is less than say  $p_{\max}$  (as counted after discretizing the cyclic order  $\alpha$ ), the  $100p\%$  percentile of  $\hat{I}_X^S(\alpha_k)$  will be the same under  $H_0$  and  $H_1$  for any  $p < p_{\max}$ . This makes it possible to compute a threshold  $\lambda_{1-p}$  for the statistical test based on the histogram of  $\hat{I}_X^S(\alpha_k)$  (see Fig. 2 (d)) as the level under which are found  $100p\%$  of the values. Thanks to the standardization applied in Eq. (7), the threshold is constant with respect to cyclic frequencies, as illustrated by the red horizontal line in Fig. 2 (e). The above threshold will be used to detect the presence of peaks, as explained in the next subsection.

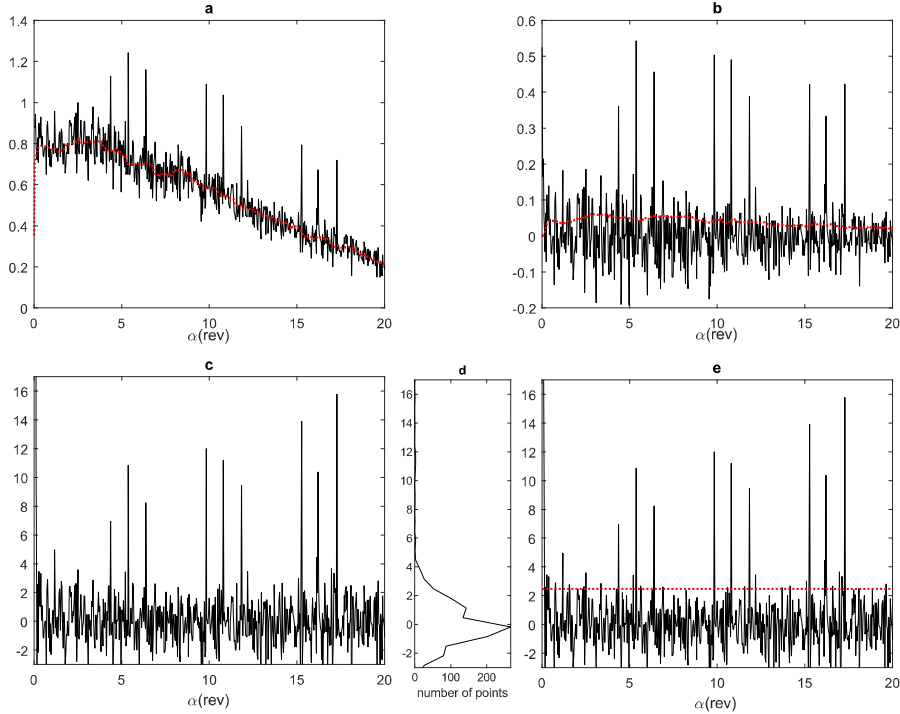


Figure 2. a) The estimated enhanced envelope spectrum (EES)  $\hat{I}_X(\alpha_k)$  of the simulated vibration signal and its running median  $\mu_{MED}(\alpha_k)$  in dashed red line. b) Centered EES after subtraction of  $\mu_{MED}(\alpha_k)$  together with the running median absolute deviation  $\sigma_{MAD}(\alpha_k)$  shown in dashed red line, c) Equalization after division by  $\sigma_{MAD}(\alpha_k)$  d) histogram of standardized EES  $\hat{I}_X^S(\alpha_k)$ , e) threshold  $\lambda_{0.9}$  (red line).

### 3.3 Design of the test statistic

The next step in the design of the hypothesis test is to detect peaks at the expected fault frequencies in the EES under  $H_1$  and to devise a measure of their intensity. It is expected that such a measure increases with the magnitude of the peaks and with their number (incipient faults are likely to produce several harmonics). Besides, the fact that the fault frequencies are subject to random jitter should be taken into account. To do so, a band  $B_1$  is first defined, centered at the theoretical fault characteristic order  $\alpha_{c_1}$ , with a deviation tolerance of  $100X\%$ , typically between  $5\%$  and  $10\%$ . The lower and upper bounds  $\alpha_1^L$  and  $\alpha_1^U$  of band  $B_1$  are thus defined as

$$\begin{cases} \alpha_1^L = \alpha_{c1} - X\alpha_{c1} \\ \alpha_1^U = \alpha_{c1} + X\alpha_{c1} \end{cases} \quad (8)$$

The highest peak in the band is theoretically defined as

$$m_1 = \max_k [\hat{I}_X^S(\alpha_k) \cdot \mathbb{1}_{B_1}(\alpha_k)]; B_1 = [\alpha_1^L; \alpha_1^U] \quad (9)$$

where the symbol  $\mathbb{1}_{B_1}(\alpha_k)$  denotes the indicator function defined on  $B_1$  having the value 1 for all elements of  $\alpha_k$  in  $B_1$  and the value 0 for all elements of  $\alpha_k$  not in  $B_1$ .

In practice, the fact that the EES is computed on a grid of cyclic frequencies might introduce a bias in the estimation of the peak magnitude (the so-called ‘‘peak-fence effect’’). In order to alleviate it, a well-known solution used in the spectral analysis is to interpolate  $\hat{I}_X^S(\alpha_k)$ , for instance by using zero-padding and/or by using a spectral window such as the flattop in the Fast-OFSC.

Once  $m_1$  is identified, a measure that represents the probability of the presence of the first harmonic of the fault,  $PPF_1$ , is calculated based on the statistical threshold  $\lambda_{1-p}$  as follows,

$$PPF_1 = \begin{cases} \frac{m_1 - \lambda_{1-p}}{m_1} & m_1 \geq \lambda_{1-p} \\ 0 & m_1 < \lambda_{1-p}. \end{cases} \quad (10)$$

With the objective of keeping only the indicative values at  $\lambda_{1-p}\%$  and setting all the others to zero. The rationale of this equation is to return a zero probability whenever  $m_1$  is less than the threshold  $\lambda_{1-p}$  and, otherwise, a value that tends to unit probability when  $m_1$  grows to infinity. In the case of the non-zero value of  $PPF_1$ , the algorithm then searches for the presence of the second harmonic in a new band  $B_2$ . In order to properly define  $B_2$ , the center of the first band is first corrected to account for the possible mismatch between the actual and the theoretical fault order by defining  $\alpha_{c_1}^{corr}$  such that  $m_1 = \hat{I}_X^S(\alpha_{c_1}^{corr})$ . Thus, the second band  $B_2$  is centered on  $\alpha_{c_2} = 2\alpha_{c_1}^{corr}$  and is given the same bandwidth as  $B_1$  (i.e. with deviation tolerance of  $100(X/2)\%$  around  $\alpha_{c_2}$ ). The second harmonic is detected if the highest peak  $m_2$  in band  $B_2$  is above the threshold  $\lambda_{1-p}$ ; it thus yielding a non-zero value of  $PPF_2$ . The algorithm then searches for the presence of the third harmonic in a band  $B_3$  centered on  $\alpha_{c_3} = 3\alpha_{c_1}^{corr} + (3/2)\alpha_{c_2}^{corr}$  where  $\alpha_{c_2}^{corr}$  is such that  $m_2 = \hat{I}_X^S(\alpha_{c_2}^{corr})$ , etc.

The general formulas describing the algorithm are resumed hereafter:

$$\left\{ \begin{array}{l} \alpha_{c_i} = \frac{i}{(i-1)} \sum_{n=1}^{i-1} \frac{\alpha_{c_n}^{corr}}{n}, i > 1 \quad (11) \\ m_i = \max_k [\hat{I}_X^S(\alpha_k) \cdot \mathbb{1}_{B_i}(\alpha_k)]; B_i = [\alpha_{c_i} - X\alpha_{c_1}; \alpha_{c_i} + X\alpha_{c_1}] \quad (12) \\ \alpha_{c_i}^{corr}: m_i = \hat{I}_X^S(\alpha_{c_i}^{corr}) \quad (13) \\ PPF_i = \begin{cases} \frac{m_i - \lambda_{1-p}}{m_i} & m_i \geq \lambda_{1-p} \\ 0 & m_i < \lambda_{1-p} \end{cases} \quad (14) \end{array} \right.$$

where  $\alpha_{c_n}$  is the center of the band  $B_n$  around the  $n$ -th harmonic.

Once the  $PPF_i$ s in all concerned bands have been calculated, an overall indicator  $PPF$  is calculated as the mean value

$$PPF = \frac{1}{n} \sum_{i=1}^n PPF_i \quad (15)$$

in order to take a final decision. In some cases, where a rolling element fault (or the inner-race fault) need to be searched, two additional left and right probabilities ( $PPF_i^r$  and  $PPF_i^l$ ) of the possible side-bands around each harmonic order must be calculated. For each harmonic and if the fault characteristic order is amplitude modulated by a sub-band order, there should be at least one prominent peak at the  $\pm\alpha_{sub}$  away from  $\alpha_{c_i}$ . In the same way as  $PPF_i$ ,  $PPF_i^r$  and  $PPF_i^l$  are calculated for each harmonic in a narrow band centered at  $\alpha_{c_i} \pm \alpha_{sub}$ .

The reason to calculate two different probabilities for the left and the right possible sub-bands is that the two sub-bands are not necessarily symmetrical, and the existence of the one does not mean the existence of the other. Thus, the combination of these two values can cause damage to the information.

Nevertheless,  $PPF$  is a normalized indicator that can take any value between zero and one.  $PPF$  it is the probability of the presence of a REB fault (with risk of  $p\%$ ). Based on the above information, it is easy to perform a statistical test: any value of  $PPF$  that is greater than the constant threshold  $\lambda_{1-p}$  will point out the emergence of the fault signature in  $100(1-p)\%$ .

But in order to make a final and definitive decision  $PPF$  is compared with a global measure of CS in the whole spectrum, which can give a decisive conclusion. This global measure of CS called ' $T$ ' is the relative error between the median of all peaks along the order axis that exceeds the statistical threshold and the constant statistical threshold  $\lambda_{1-p}$ .

The median of all peaks along the order axis that exceeds the statistical threshold called " $GM_{CS}$ " –the abbreviation for Global Measure of CS- is defined as:

$$GM_{CS} = \frac{\sum_{k=1}^{k_{max}} \hat{I}_S(\alpha_k) \cdot \mathbb{1}_{[\hat{I}_X^S(\alpha_k) > \lambda_{1-p}]}}{N_b} \quad (16)$$

Then the normalized version of the global version of CS called "the threshold  $T$ " is defined as:

$$T = \frac{GM_{CS} - \lambda_{1-p}}{GM_{CS}} \quad (17)$$

where  $N_b$  is the number of points exceeding  $\lambda_{1-p}$  all over order axis,  $k_1$  and  $k_{max}$  are the first and the last order indices in the order axis. The  $T$ -threshold value is a normalized version of  $GM_{CS}$  which resembles, in its way of calculation, the DCS in Ref. [19], but only with the addition of the indicator function  $\mathbb{1}_{[\hat{I}_X^S(\alpha_k) > \lambda_{1-p}]}$ , to compute only the peaks greater than constant statistical threshold  $\lambda_{1-p}$ .

Once the  $T$ -threshold is calculated, a comparison is made with  $PPF$  in order to detect the sought fault. If  $PPF$  has a higher value than  $T$ , the peaks are quite significant with respect to the noise and other peaks along the order axis, hence the fault exists.

The null hypothesis test relative to our case originating from the comparison between  $PPF$  and  $T$  can be written as:

“Reject the null hypothesis H0 if:

$$PPF \geq T \quad (18)$$

with  $T$  given by Eq. (17) and  $PPF$  by Eqs. (14-15). Eq. (18) eventually takes the following form (see Appendix A):

$$\frac{1}{N} \sum_{i=1}^N \frac{1}{m_i} \leq \frac{1}{GM_{CS}} \quad (19)$$

It easily allows performing a statistical test: according to the decision rule, any value of  $PPF$  that is greater than the  $T$ -threshold will indicate that the signature of the fault is detected.

The proof of Proposition Eq. (19) is based on observing that under the null hypothesis test  $H_0$  the quantity asymptotically follows a nonparametric distribution that has a constant bias and variance all over the cyclic order axis. It also remembers that this test is true almost everywhere.

In this hypothesis test  $GM_{CS}$  appears directly in the rejection region whereas the threshold  $\lambda_{1-p}$  does not figure directly but it is important to choose  $m_i$  that are greater than  $\lambda_{1-p}$ .

The complete flow diagram for the algorithm described in this section is shown in Fig.3

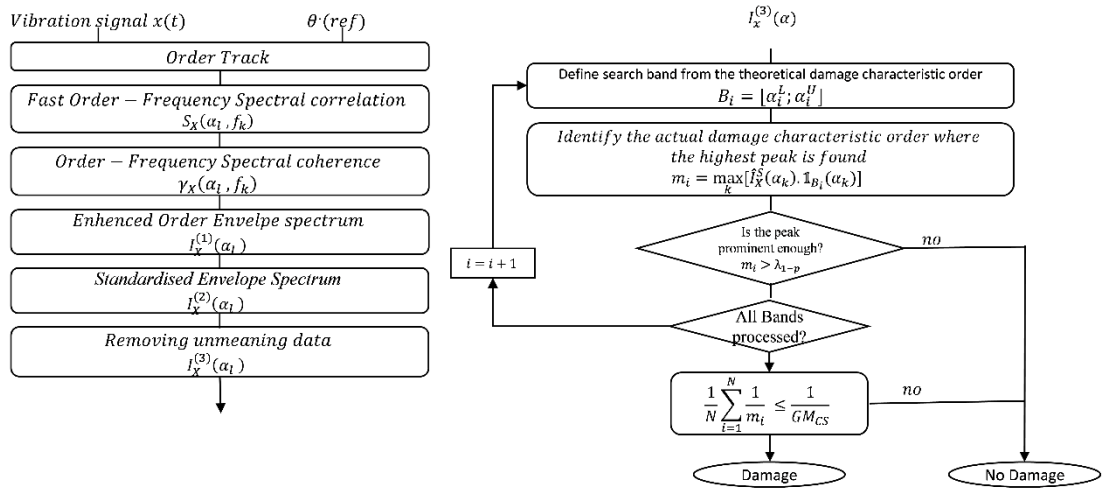


Figure 3. Complete algorithm flowchart

#### 4 Experimental validations

The ability of any method to detect a bearing fault must be validated on real signals. In the present paper, four benchmarks are used. The first one is provided by NASA, from the Intelligent Maintenance Systems (IMS), University of Cincinnati [31], the second one is provided by the CRWU Bearing Data Center [32] while the third one is provided as supplementary material in Ref. [33]. These databases are widely used to test new algorithms by comparing their efficiency with existing techniques, similarly to those cited in reference [24]. The NASA database is a run-to-failure test, used to reflect how the proposed indicator works with the development of a fault. The second database provides multiple fault types, i.e. rolling element, cage inner-race, and outer-race fault, and it is used to illustrate the proposed method and to compare the proposed algorithm to those existing in the literature. The third and fourth databases are used to illustrate the diagnostics of rolling element bearings under the varying regime.

## 4.1 Constant speed case

### 4.1.1 Algorithm illustration

To illustrate the proposed algorithm, a simple case is considered wherein the four characteristic fault orders are already known. This analyzed signal is the record 105DE of the (CRWU) Bearing Data Centre, which contains an inner-race fault. The sampling frequency is 12 kHz and the record duration is 10 s. The rotations speed is assumed constant, about 29.95 Hz. As explained in Ref. [24], this signal is easily diagnosable and it should, therefore, be considered as a preliminary test for the proposed algorithm. A visual inspection of the signal in Fig. 4 shows a symptomatic series of impulses at BPOI, as expected from the model of section 2. Based on the bearing geometry, the characteristic inner-race fault order is 5.4152. From now on, the coefficient 5.4152 will be denoted as the BPOI (ball-pass order on the inner-race).

As explained before, the first step of the algorithm starts with the computation of the Fast-OFSC [26]. In what follows, the window length in the Fast-OFSC is set to  $N_w = 2^7$  to achieve a frequency resolution  $\Delta f$  of 100 Hz. The maximum cyclic order  $\alpha_{max}=20$  is selected to include at least three harmonics of the BPOI since the number of harmonics provides an indication of the fault severity. The standardized EES is computed over the full frequency range [0;6000Hz], hence referred to a “wideband” envelope spectra. In this application only three narrow bands ( $n=3$ ) with deviation tolerance of  $X=5\%$  are used. Since the reference [24] reported a deviation from the calculated frequency up to 1-2% for this database, a deviation tolerance equal to 5%(2.5% around the characteristic fault frequency) is used.

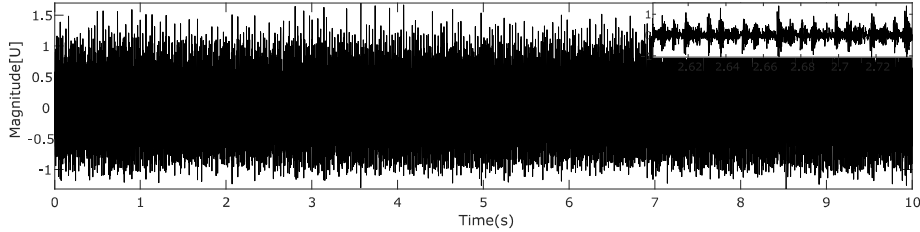


Figure 4. Raw time signal of record 105DE, and its zoomed portion

As seen in Fig. 5, the standardized EES displays the expected symptomatic fundamental and harmonics of the inner-race fault ( $\alpha_{BPOI}=5.4152$ ) with sidebands spaced at the shaft order ( $\alpha_{\dot{p}}=1$ ); the shaft speed fundamental order is also present. The statistical threshold  $\lambda_{1-p}$  (red dashed horizontal line) with a rate of false alarm  $p = 0.01$  (0.1%), is found equal to 0.18. It is noteworthy that this method perfectly preserves the diagnostic information that nicely appears with a significant overrun of the 0,1% statistical threshold. This figure illustrates how the algorithm next tracks the first (resp. second and third) harmonic of the inner-race fault as well as the shaft rotation sidebands. In order to perform the nonparametric approach, any value of the  $PPF$  that is greater than or equal to the constant threshold  $\lambda_{1-p}$  will point out the emergence of the harmonic  $i$  of the fault signature in 100(1-p)% of the cases. Then, the fault probability  $PPF$  assigned to the inner-race fault order and the left and right probabilities,  $PPF_l$  and  $PPF_r$ , assigned to the side-bands are calculated; their values are respectively 0.9, 0.87 and 0.8.

Since the detection threshold  $T$  is equal to 0.5, the inner-race fault is detected according to the decision rule provided by Eq. (18).

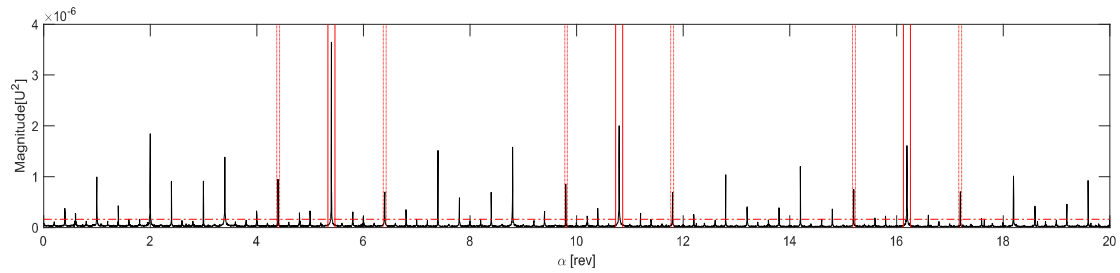


Figure 5: Standardized EES  $\hat{f}_x^s(\alpha_k)$  of the raw signal together with the  $\lambda_{0.99}$  threshold (red dashed line). Bands (in red line) and side-bands (in vertical red dashed line) used for the calculation of  $PPF$  (harmonics of the inner-race race fault order) and  $PPF_r$  and  $PPF_r$  (side-bands at shaft rotation)

#### 4.1.2 Performance Evaluation of IMS Database in Order to Reflect Fault Severity Response

This subsection illustrates the application of the autonomous diagnosis method to a run-to-failure test case. The test is performed at a constant speed of 2000 rpm driven by an AC motor on a test rig under a radial load of 6000 lbs. The bearing test rig hosts four identical bearings of type Rexord ZA-2115 in the same shaft (see Fig. 6). Based on their characteristics (16 rollers, pitch diameter of 7.15 cm, roller diameter of 0.84 cm and the contact angle of 15.170), the four fault characteristic orders are calculated in Table 1.

The second dataset from those provided in the download file has been used. It is composed of 984 files, and each file is composed of 20,480 samples. A one-second acquisition has been made every ten minutes. The sampling frequency is 20.48 kHz.

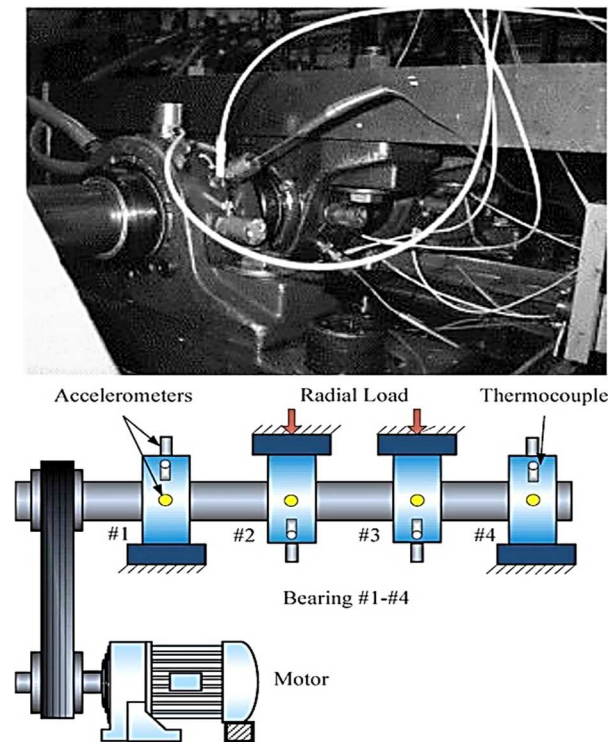


Figure 6. Bearing test rig and sensors placement [34].

Table 1. Bearing fault characteristics orders.

Ball pass order on the outer-race (BPOO)	7.08
Ball pass order on the inner-race (BPOI)	8.91

Ball spin order (BSO)	8.34
Fundamental train (cage) order (FTO)	0.45

Table 2. Dataset description

	Files number	Channels number	Endurance duration	Signals duration	Announced damages
Dataset 2	984	4	9840 min 6 days 20h	16 min	Bearing 1: outer race

Table 2 summarizes the information of the used dataset. A detailed explanation of this dataset is given in [35].

Assuming that the type of fault is unknown, the autonomous algorithm is run to calculate the probability of the presence of the four possible faults listed in Table 1. The parameters to calculate the Fast-OFSC are as in section 4.1, i.e.  $\alpha_{max}$  is equal to 36 orders. The EES  $\hat{I}_X^S(\alpha)$  is computed over the full frequency range [0;10.24 kHz], the rate of false alarm  $p = 0.001$  (0.1%), and only three narrow bands ( $n=3$ ) with deviation tolerance of  $X=5\%$  are used.

Figure 7 (a) displays the EES  $\hat{I}_X^S(\alpha)$  estimated on accelerometer #1 for the 984 signals recorded during the run-to-failure test (from the beginning to the failure). It is seen that the fundamental order of the BPOO is present from the beginning of the test (probably due to close distance between accelerometer #1 and the bearing), yet its related harmonics appear after approximately 3.4 days, which is more likely to be indicative of a fault.

The four *PPF* probabilities associated with each bearing fault are displayed in Fig. 7(b). It is seen that they are all stationary in the first half of the test and all remain well below the  $T$ -threshold. Therefore, the probability of the presence of a REB fault is found to be zero in this stage (with risk 0.01). Next, except for the FTO which remains stationary, all probabilities show a marked increase after 3.4 days. However, this is also the case for the threshold  $T$  - a global measure of the fault existence-- and only the probability of the outer-race fault exceeds the decisive threshold. This indicates a high probability of having an outer-race fault and zero probability of having other types of faults.

This result matches the visual interpretation already provided. The short-term fluctuation of the BPOO's probabilities as a function of measurement time (Fig. 7 (b) in blue) is due to the varying number and varying magnitudes of the peaks in the EES.

Figure 8 displays the fault detection probabilities of each bearing fault type calculated for each accelerometer after thresholding the values below the significance level  $T$  - zeros all the *PPF* under the  $T$ -threshold. The outer-race fault - and only this fault -- is detected in all accelerometers, but at different dates which are reported in Table 3. Without surprise, the initiation of the fault is first detected on accelerometer #1 which is located on the faulty bearing. The chronology of detection for the other sensors is less obvious, since for instance the farthest accelerometer #4 is the second one to detect the fault; this might be explained by the fact that accelerometer #4 is placed on the same frame as accelerometer #1, whereas accelerometers #2 and #3 are on a different frame and with an opposite direction (thus with inverted radial load) as indicated in Fig. 8. Overall, accelerometers #1 and #4 also reach higher probability than accelerometers #2 and #3. Nevertheless, the presence of an outer-race fault is detected on all sensors with a high probability.

In conclusion, the goal is reached and the indicator prosperously matched the visual interpretation extracted from the EES map and reflected the fault severity. As a summary, the results are quoted in Table 3.

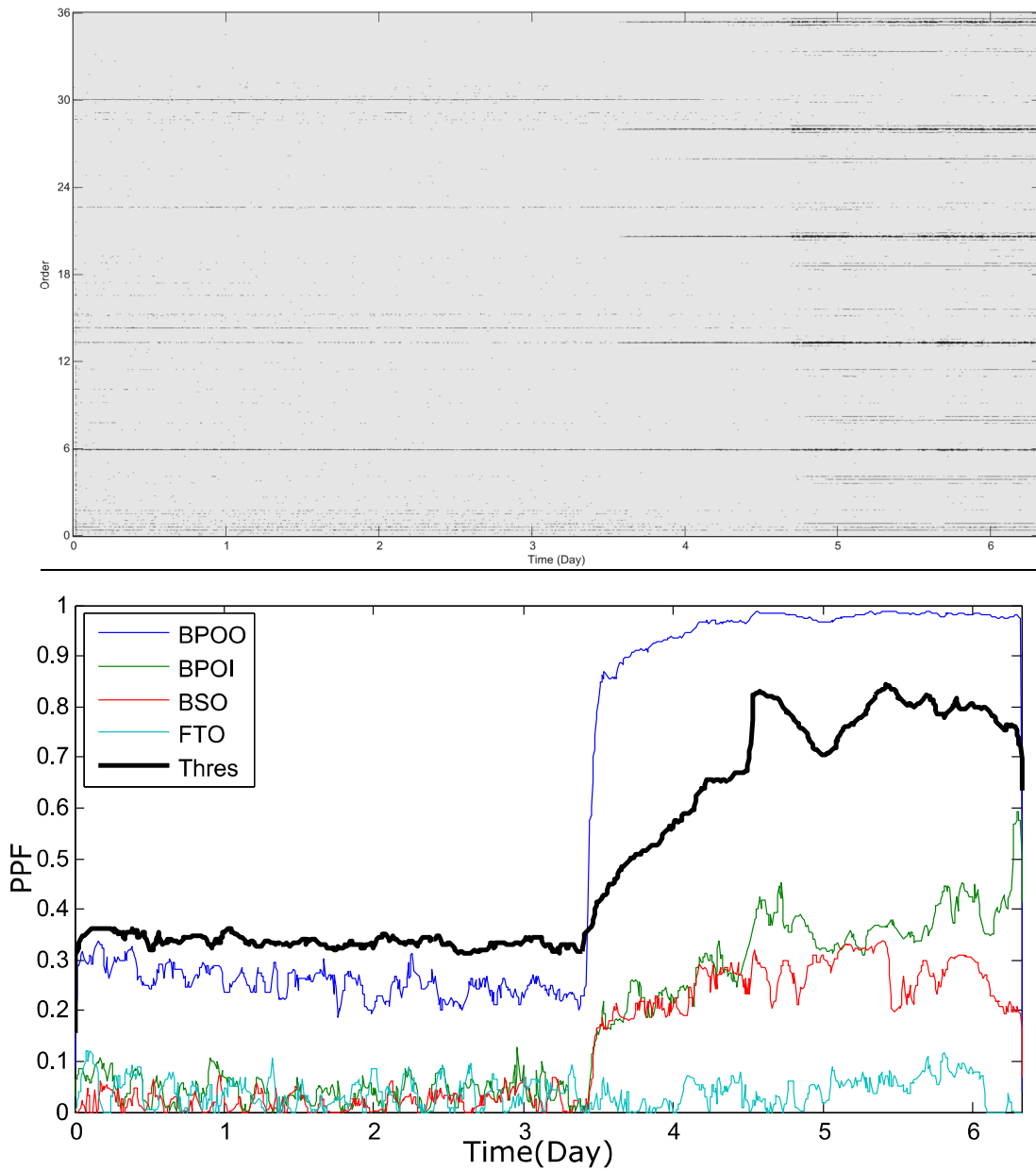


Figure 7. a) Evolution of the enhanced envelope spectrum  $\hat{I}_x^{\alpha}(\alpha)$  and b) of the detection probability  $PPF$  of BPOO, BPOI, BSO and FTO during the test. Also shown in (b) T, the global measure of CS

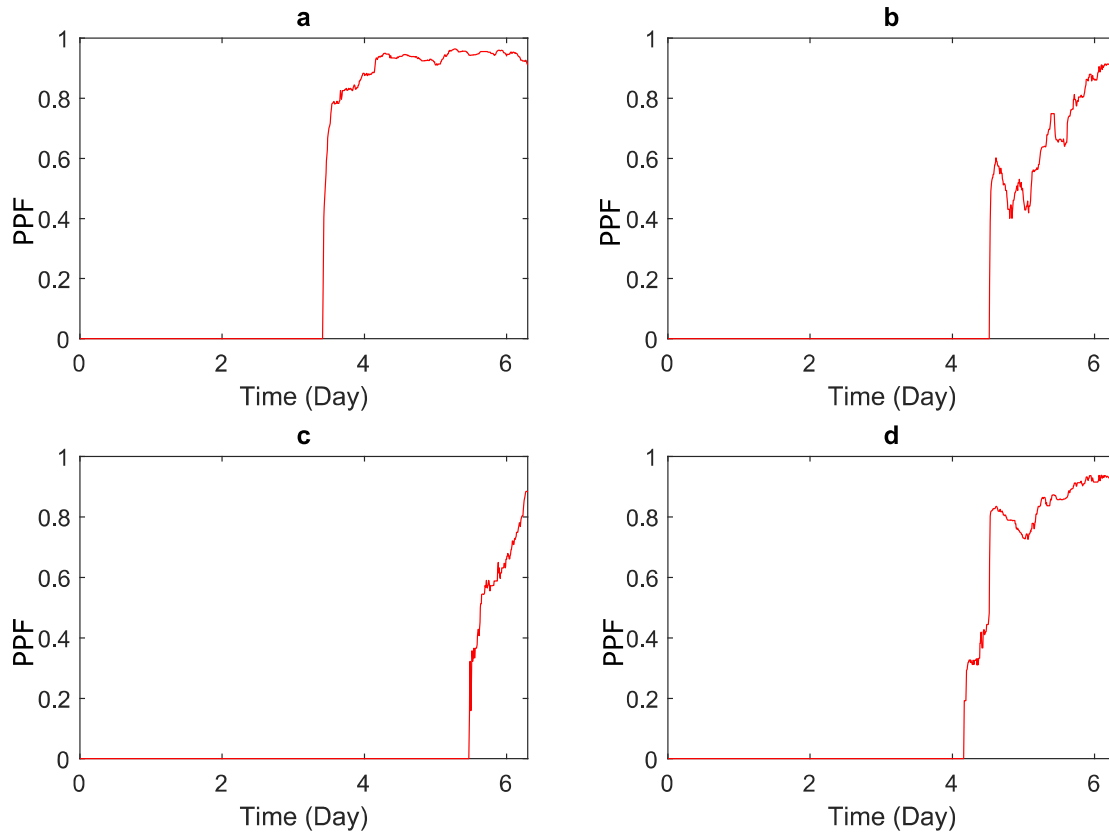


Figure 8. Fault detection probabilities PPF of each bearing fault after thresholding the values below the  $T$ -threshold calculated for accelerometer : a) #1 b) #2 c) #3 d) #4 as numbered in Figure 6.

Table 3. Dates of the first detection of outer race fault using  $PPF$  for accelerometer: #1, #2, #3 and #4

	Acc#1	Acc#2	Acc#3	Acc#4
Results	3.4 days	4.5 days	5.4 days	4.1 days

#### 4.1.3 Performance Evaluation in the CWRU database.

The performance of the proposed indicators is now evaluated on the bearing signals provided by the CWRU database. The CWRU database has been used in many references (e.g. [24], [26], [36]) and can be considered as a reference to test newly proposed algorithms and compare them against the state-of-the-art; this is despite several drawbacks of the database that have been highlighted in Ref. [24]. The experimental setup consists of a 1.4914 kW, reliance electric motor driving a shaft on which a torque transducer and encoder are mounted. Torque is applied to the shaft via a dynamometer and electronic control system. Four types of vibration signals are collected (normal, ball fault, inner-race fault, and outer-race fault), acquired by accelerometer sensors under different operating loads and speeds. The bearing type is a deep groove ball bearing SKF6205-2RS JEM; its fault characteristic orders are given in Table 4.

In this study, the drive end data-set category with sampling frequency 12 kHz have been analyzed and compared with results provided by Ref. [24], which presents a critical analysis of the CWRU database. Information for all 64 data sets used is shown in Table 5.

Table 4. Bearing fault characteristics orders.

Ball pass order on the outer-race (BPOO)	3.584
Ball pass order on the inner-race (BPOI)	5.415
Ball spin order (BSO)	4.713
Fundamental train (cage) order (FTO)	0.398

Table 5. The 12 kHz drive end bearing faults data sets used besides the normal data (48 kHz).

Fault types	Data sets name
Inner-race	105,106,107,108,169,170,171,172,209,210,211,212,3001,3002,3003,3004
Ball	118,119,120,121,185,186,187,188,222,223,224,225,3005,3006,3007,3008
Outer-race (centred)	130,131,132,133,197,198,199,200,234,235,236,236
Outer-race (orthogonal)	156,158,159,160,258,259,260,261
Outer-race (opposite)	144,145,146,147,246,247,248,249
Normal data	97,98,99,100

Two methods have been applied to the 64 data sets in this study. Since in the present work the nature of the fault is assumed unknown, it is necessary to systematically test, for each data set in Table 5, the possibility of existence of faults on the inner-race, the outer race, and on the balls.

The tables in Appendix B (Table B.1, Table B.2 and Table B.3) collect the results of the proposed method and the one proposed by Klausen *et al.* in Ref.[25]. Included in these tables are the estimated probabilities or values of the presence of faults as well as the  $T$ -threshold value, of each raw data-set.

In the following, results are summarized in confusion tables (tables 6, 7 and 8) to facilitate comparisons with results provided in Ref. [24]. To do so, the following strategy is used: for each data set, only the faults with the highest probability (for the proposed method) or score (for Ref.[25]) are considered.

#### 4.1.3.1 Analysis with a concurrent method

In order to verify the efficiency of the proposed method, it is compared to a recently autonomous method recently proposed by Klausen *et al.* in Ref. [25]. The method consists of the following steps. First, the signal is bandpass filtered in several bands defined by local maxima in the spectrum. Next, the ES in each sub-band signal is calculated. Finally, a score  $S(H)$  is calculated in a predefined narrow band of the ES centered at the expected fault frequency. The score is defined as follows:

$$S(H) = \begin{cases} \left(\frac{M_h}{3N}\right) \times H^2, & M_h > 3N \\ 0, & \text{otherwise} \end{cases} \quad (20)$$

where  $M_h$  is the maximum spectral amplitude in the band,  $H$  is the harmonic number of the expected fault frequency and  $N$  is the noise level estimated from

$$N = \frac{1}{n-1} \left( \sum_i Y(i) \cdot \mathbb{1}_{[f_{n1} \leq f(i) \leq f_{n2}]} - Y(I) \right) \quad (21)$$

where  $Y(i)$  is the amplitude of the ES of the raw signal,  $f(i)$  is the frequency variable at the  $i$ -th bin,  $Y(I)$  is the amplitude of the most prominent harmonic peak in the ES,  $f_{n1}$  and  $f_{n2}$  are respectively the upper and lower bound of the search band.

The detailed results obtained after application of this algorithm to the CWRU dataset are presented in Appendix B (Table B.3) and a summary is given hereafter in Table 6. It is worth noting that the parameters of the algorithm are very similar the ones in Ref.[25].

Table 6. Percentage of detection of the method of Ref. [25] applied to the DE 48 kHz files in CWRU dataset.

Classified as \ Detected	Inner-race	Outer-race	Ball
Outer-race	6.25	78.57	56.25
Inner-race	75	7.1429	43.75
Ball	6.25	0	0
No fault detected	12.5	14.2857	0

The percentages obtained by the autonomous detection of the BPFO, BPFI, and BSF are respectively 78.57%, 62.5% and 0% as shown in Table 6, while it was respectively 92%, 75% and 56% obtained by visual human analysis reported in Ref. [24]. It is clear that the rate of autonomous detection is lower than that given by the human analysis (visual inspection of the ES provided in Ref.[24]).

It is believed that the reasons for this discrepancy are due to several factors mainly related to the preprocessing of the signals. In order to improve the diagnosis results, a few modifications have been applied to the original algorithm. First of all, the Kurtogram has been found useful to better identify the optimal band-pass filter. Next, the squared ES has been used instead of the (amplitude) ES for the reasons already cited in section 2. Finally, the predefined detection threshold provided by the proposed method will be used since it is essential for analyzing the results. After applying these modifications, the diagnosis results showed some improvements as shown in Table 7.

Even though, this score may be misleading in case of coarse frequency resolution when a peak in the ES appears in multiple frequency bins instead of one frequency.

Table 7. Percentage of detection of the method in Ref. [25] applied to data sets in Table 5, after minor modifications of the method.

Classified as \ Detected	Inner-race	Outer-race	Ball
Outer-race	6.25	82.1429	50
Inner-race	81.25	3.5714	43.75
Ball	0	0	6.25
No fault detected	12.5	14.2857	0

#### 4.1.3.2 Analysis with the proposed algorithm

The proposed method is now applied to the same dataset. The parameters of the Fast-OFSC are as given in section 4.1. The maximum cyclic order  $\alpha_{max}$  is equal to 21, the rate of false alarm  $p = 0.001$  (0.1%), the deviation tolerance of 5% of the theoretical fault characteristic order. Table in Appendix B gives the detailed diagnosis results.

The obtained results reported in the Table 8 show a significant improvement over the results shown in Table 6 and Table 7. This is due to the use of the spectral coherence (which has been verified to never performed worse than the reference methods of Ref. [24], as verified in Ref. [26]) and of the resulting ESS,  $\hat{I}_X^S(\alpha)$ ; the latter clearly highlights the dominant harmonics of the BPOO, BSO, and BPFO with sidebands at the FTO and at the shaft rotation, contrary to the classical SES that has a poorer SNR [26].

Table 8 Percentage of detection of the proposed algorithm in the CWRU database.

Classified as	Inner-race	Outer-race	Ball
---------------	------------	------------	------

Detected			
Outer-race	0	96.4286	18.75
Inner-race	93.75	0	12.5
Ball (and Cage)	0	0	50
No fault detected	6.25	3.5714	18.75

The proposed indicator causes much higher percentage of 'no fault detected' for the rolling element faults than the indicator of Ref.[25] and that refers to the presence of a possible bias (as typically produced by transient disturbances in the signal or the presence of unexplained nonstationarities) in the squared envelope spectrum lead to false indication when using the method of Ref. [25] (Revise figures in Ref. [24] of the following cases: record 125DE, record 174DE, record 191DE, record 203DE). while in the proposed method the false alarm was avoided by standardizing the EES using Eq. (7), in order to force the EES to have a constant probability distribution with respect to the cyclic order. For the latter reason the proposed method indicates much higher percentage of 'no fault detected' for the rolling element faults. It is noteworthy that in the cases of rolling element fault in the CWRU database, the automated methods did not show the expected results. This is probably due to the fact that these signals are either misclassified in the database or very noisy (some signals exhibit BPFO or of BPFI signatures as presented in the tables) or that the fault did not produce the expected signature (several peaks appear in the spectral coherence which do not represent any of the known faults). The same issues are mentioned in Ref. [24], where the visual inspection led to similar results. In conclusion, the success of our indicator is consistent with to the visual inspection.

## 4.2 Varying speed case

### 4.2.1 Real-world signal provided by Ref.[33]

The methodology is now applied on real vibration signals in three cases associated with three distinct REB faults. The dataset used in this paragraph is provided as supplementary materials in Ref. [33]. Vibration signals were collected using a Ploytec laser vibrometer from a small test rig with three distinct pre-fabricated bearing faults (in outer-race, inner-race and ball). The test rig consists of an induction motor of 0.372 kW with speed controller, followed by a simple power transmission chain which includes faulty REBs. The duration of signals is 21 s with a sampling frequency of 50 kHz. The rotating speed was manually controlled in order to keep the resulting profile varying between 10 and 20 Hz during the 21 s record. The bearing fault characteristic orders are reported in Table 9. More details about the experimental protocol can be found in the reference source [33].

In the present paper, the same portion of signals (from  $t = 5$  s to  $t = 15$  s) and the same parameters calculate the Fast-SC as in Ref. [37] have been used in order to allow a fair comparison of results. The standardized EES is computed over the full frequency range,  $\alpha_{max}$  is equal to 17 orders, and three narrow bands ( $n=3$ ) with deviation tolerance of  $X=5\%$  are used.

The speed profiles and acceleration signals for experiment 1, 2 and 3 are displayed in Fig. 9. The EES of the proposed method are displayed in Fig. 10 (a, b, c) and its zoomed version Fig.11 for experiments 1-3. The outer-race fault signature is clearly presented in the EES through three spectral lines located at the outer-race fault order. The inner-race fault also shows distinctly the BPOI, with several sidebands at the shaft speed which correspond identically to the description of such a fault in section 2. As previously mentioned in many references [26], [33], [37], the BSO is missing in the ball fault signature, yet the ball fault

signature is present in the EES through several visible harmonics of the cage order. The average computational time of the algorithm was about 5.63s. According to the decision rule given in Eq. (18), any value of the PPF greater than the decision threshold  $T$  (global measure of SC) will point out the emergence of the fault signature in the EES. The returned results are as follows:

- for experiment 1: only the outer-race is detected with  $PPF(BPOI) = 0.5934$  and  $T = 0.2931$ .
- for experiment 2: only the inner-race is detected with  $PPF(BPOO) = 0.6984$  and  $T = 0.2931$ .
- for experiment 3: only the ball fault is detected with  $PPF(FTO) = 0.8759$  and  $T = 0.2931$ .

The fault detection probabilities for each fault type and for each experiment are displayed in Table 10. In conclusion, the obtained results match identically those provided with the visual inspection in Ref [37] confirming the efficiency of the proposed method.

Table 9 Bearing fault characteristics orders.

Ball pass order on the outer-race (BPOO)	3.592
Ball pass order on the inner-race (BPOI)	5.409
Ball spin order (BSO)	2.376
Fundamental train (cage) order (FTO)	0.399

Table 10. Fault detection probabilities for each fault type calculated for experiments 1, 2 and 3.

	PPF (BPOO)	PPF (BPOI)	PPF (BSO)	PPF (FTO)	$T$
Experiment 1	0.6980	0	0.1586	0.2701	0.2709
Experiment 2	0.1355	0.5934	0	0.0274	0.2931
Experiment 3	0.2773	0.0684	0.2649	0.8759	0.2807

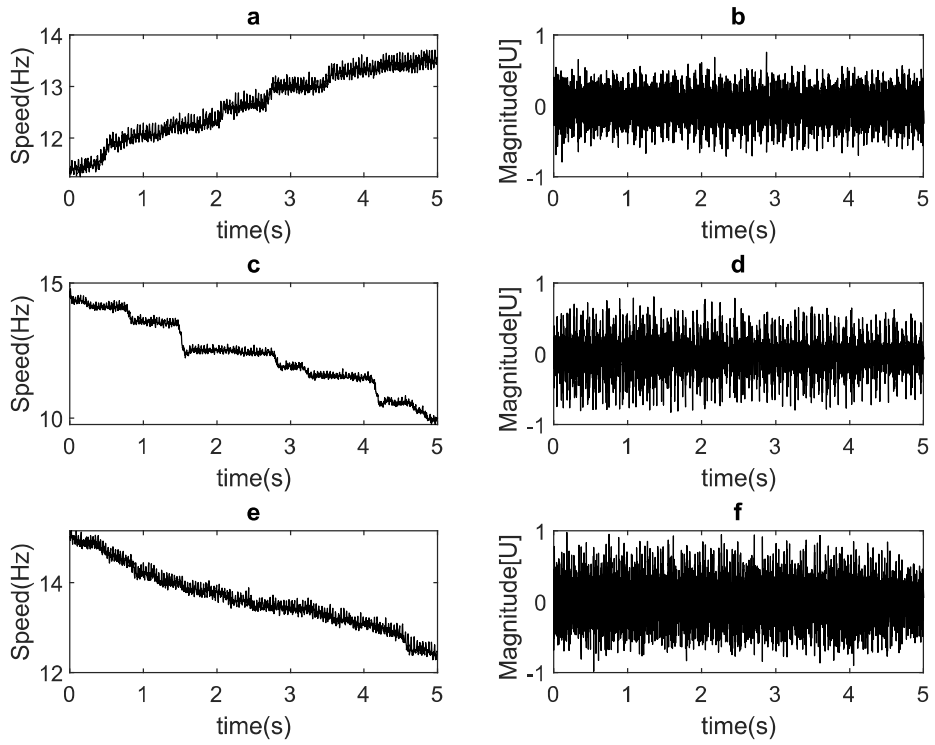


Figure 9. Experiment 1: (a) speed profile, (b) acceleration signal. Experiment 3: (c) speed profile, (d) acceleration signal. Experiment 2: (e) speed profile, (f) acceleration signal.

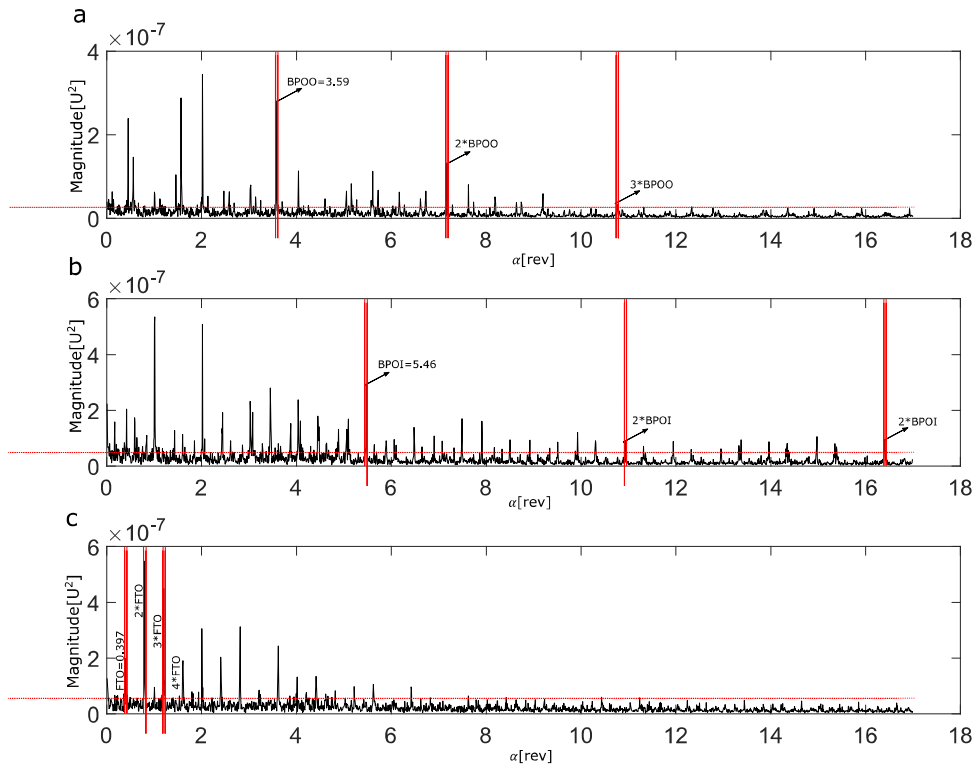


Figure 10. Standardized EES  $\hat{I}_k^S(\alpha_k)$  of the raw signal together with the  $\lambda_{0.999}$  threshold (in red horizontal line). Bands (in red vertical line) used for the calculation of *PPF* for a) experiment 1 b) experiment 2 c) experiment 3.

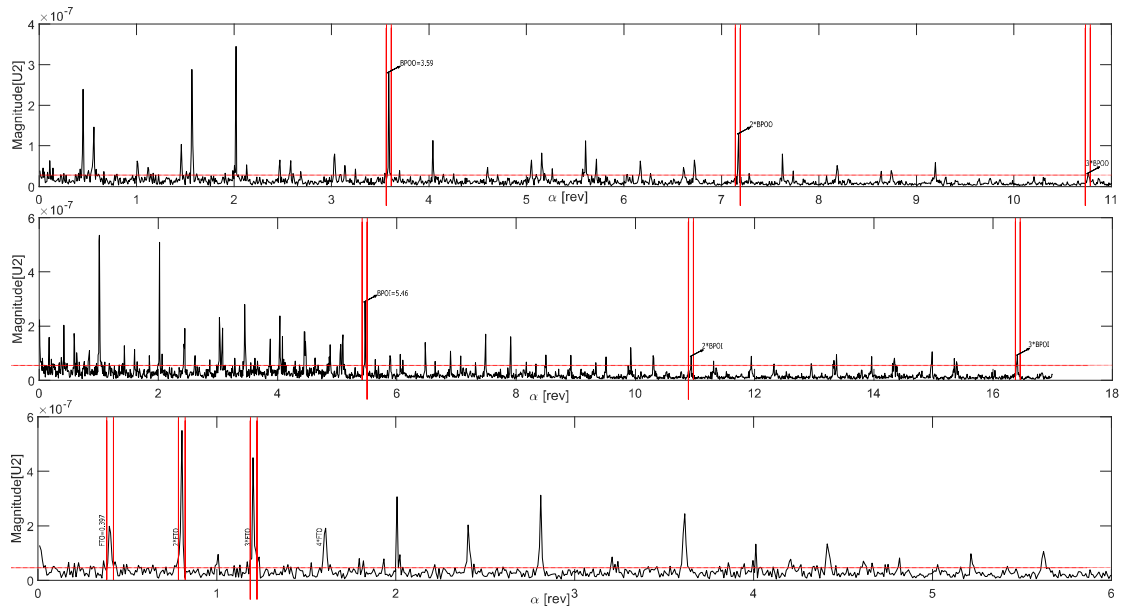


Figure 11. A zoomed version of figure 10

#### 4.2.2 Real-world signals collected from the test rig located at LVA

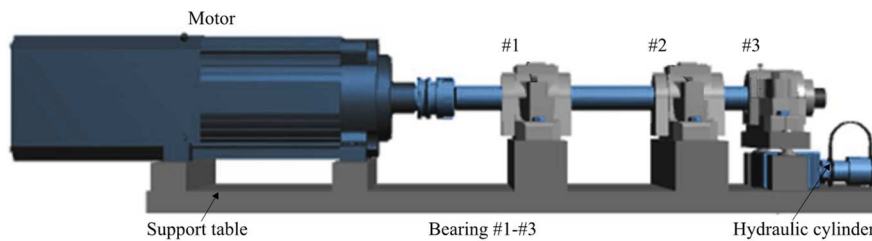
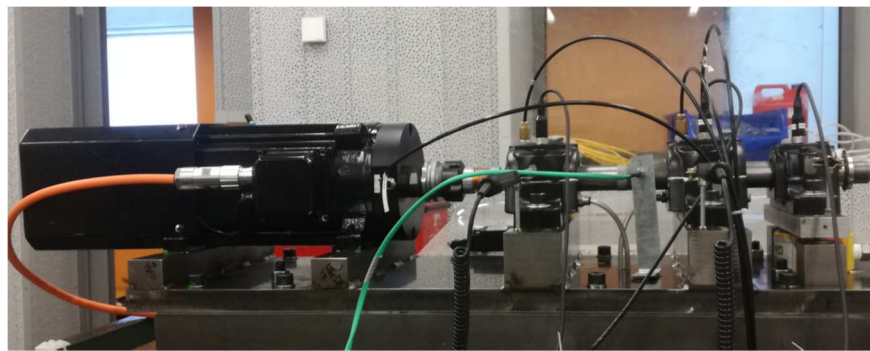


Figure 12. Test rig located at LVA.

Experimental tests have been conducted on the simple test rig of Fig. 12 that is located at LVA<sup>1</sup>. The test rig comprises an electrical motor (spindle motor iSA 3600) supplied by a variable-speed drive to control the motor speed, followed by a shaft line with three bearings. One of those bearings (denoted as #3) has an outer-race fault. Values of fault characteristic orders are given in Table 11. An optical keyphasor of type “Brawn” is fixed close to bearing 2 to measure the rotational shaft position. In addition, three accelerometers are respectively mounted on bearings #1, #2 and #3 in the Z-direction to measure the produced vibrations. The sampling rate is set at 52.1 kHz.

<sup>1</sup> Laboratoire Vibrations Acoustique, University of Lyon, France.

Two experimental tests are taken into account to test and to compare the proposed method with that proposed in Ref. [25]. First, experimental tests are conducted wherein three different constant speeds are imposed by the speed drive during 10 s. Figure 13 illustrates the EES of the raw signal measured by accelerometers Acc3 at the chosen speeds 800, 1500 and 3500 rpm. Almost the same results are obtained from the SES; hence only the EES is provided. In the second experiment, a run-up (from 500 to 3500 rpm), a random speed profile (between 500 to 3500 rpm) and a run-down (3500 to 500rpm) are imposed to the electric motor over 10s; the acquired acceleration signals are displayed in Fig. 13 together with their corresponding speed profiles.

In what follows, the window length in the Fast-OFSC is set to  $N_w = 2^7$ , the maximum cyclic order to  $\alpha_{max}=17$ , the EES is computed over the full frequency range and three narrow bands ( $n=3$ ) with deviation tolerance of  $X=5\%$  are used as parameters of the proposed method.

For the first experimental test, the outer race bearing fault signature appears clearly in the EES and the SES at the expected fault order with a significant overrun compared to the other orders. As expected, both the proposed method and the one proposed in Ref. [25] successfully detect the presence of the outer-race fault. When applied to the signal of 800 rpm, the proposed method gives a PFI equal to 0.871 while  $T$  is equal to 0.512; therefore, the outer race fault exists relating to the decision rule given in Eq. (18). The method of Ref. [25] gives a value equal to 255.034 which is higher than the value obtained on the healthy bearing signal with the same speed (56.0682). Table 12 summarizes the diagnosis results on signals of test 1.

For the second experimental test, only the EES succeeds in detecting the outer race fault symptoms while the ES used in Ref. [25] fails for the three signals. The obtained results are reported in Fig. 15 and Fig. 16. Peaks at the BPOO and its harmonics appear only in the EES while they are absent from the ES (See Fig.16). This is due to the high variability of the speed in this test. Those are cases where the ES is insufficient to accurately detect the REB fault. Therefore, it may give poor results in the case of modest speed variations and fails in large speed variations. On the other hand, the outer race fault signature appears clearly in the EES and consequently, the proposed method returns a correct diagnosis. These results are reported in Table 13. Based on these results and the decision rule of Eq. (18), the outer race fault is declared present in all signals of this test.

In conclusion, choosing the optimal representation that reveals the diagnostic information of bearing failure is crucial because the success of automated diagnostic methods strongly depends on it.

Table 11. Bearing fault characteristics orders.

Ball pass order on the outer-race (BPOO)	3.592
Ball pass order on the inner-race (BPOI)	5.409
Ball spin order (BSO)	2.376
Fundamental train (cage) order (FTO)	0.399

Table 12. Constant speed outer race bearing fault analysis results using the method of Ref.[25] and the proposed method.

	800 rpm	1500 rpm	3500 rpm
Proposed method	PFI=0.871	PFI=0.901	PFI=0.692
	$T=0.512$	$T=0.868$	$T=0.489$

Table 13. Variable speed outer race bearing fault analysis results using the proposed method.

	Run-up	Random	Run-down
Proposed method	PFI=0.698	PFI=0.593	PFI=0.5901
	$T=0.242$	$T=0.301$	$T=0.289$

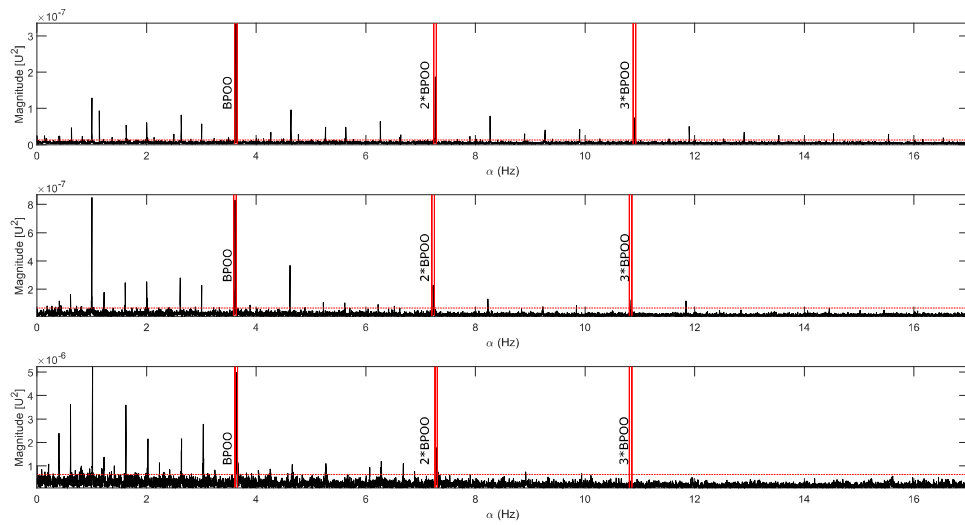


Figure 13. Standardized EES  $\hat{I}_X^S(\alpha_k)$  of the raw signal together with the  $\lambda_{0.999}$  threshold (in red dotted horizontal line). Bands (in red vertical line) used for the calculation of PPF for signals at a) 800rpm b) 1500rpm c) 3500rpm.

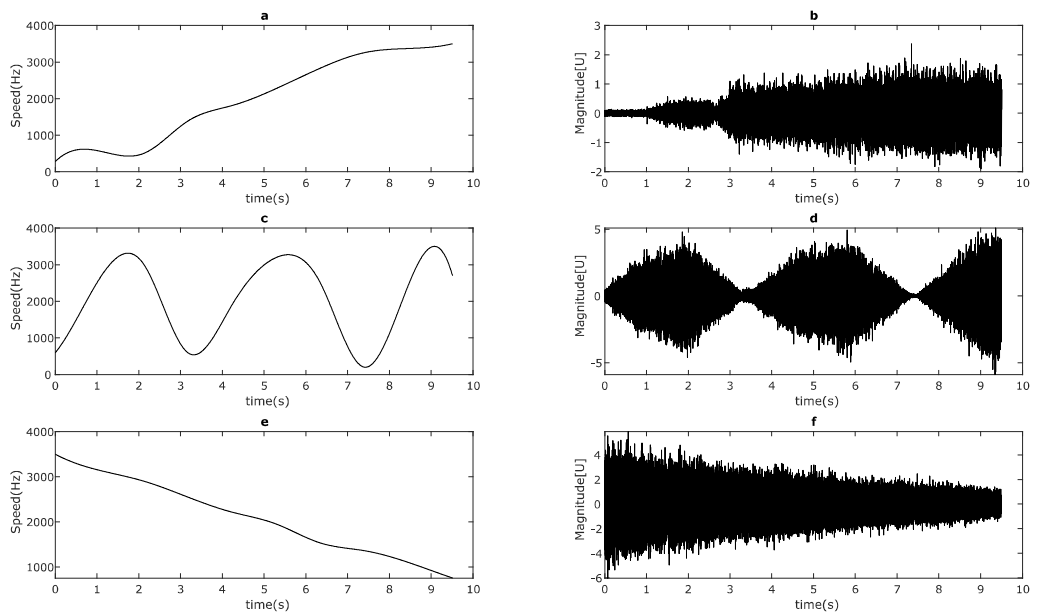


Figure 14. (a) Run-up speed profile and (b) its corresponding acceleration signal. (c) Random speed profile and (d) its corresponding acceleration signal. (e) Run-down speed profile and (f) its corresponding acceleration signal.

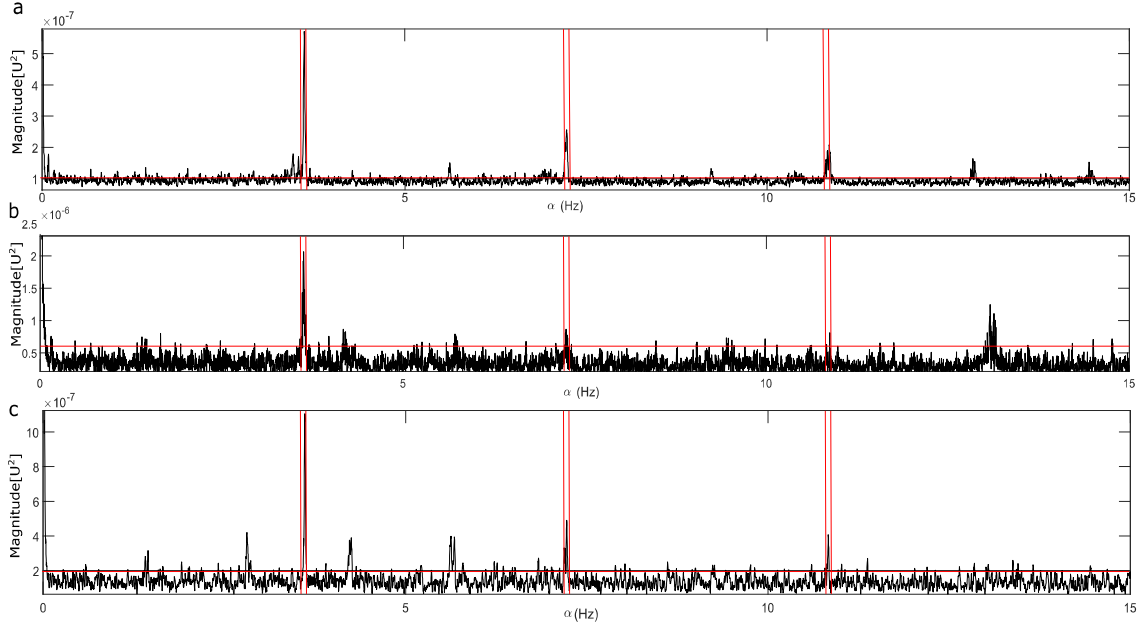


Figure 15. Standardized EES  $\hat{f}_X^{\lambda}(\alpha_k)$  of the raw signals of the Figure 14 together with the  $\lambda_{0.999}$  threshold (in red horizontal line). Bands (in red vertical line) used for the calculation of PPF for a) run-up b) random and c) run-down.

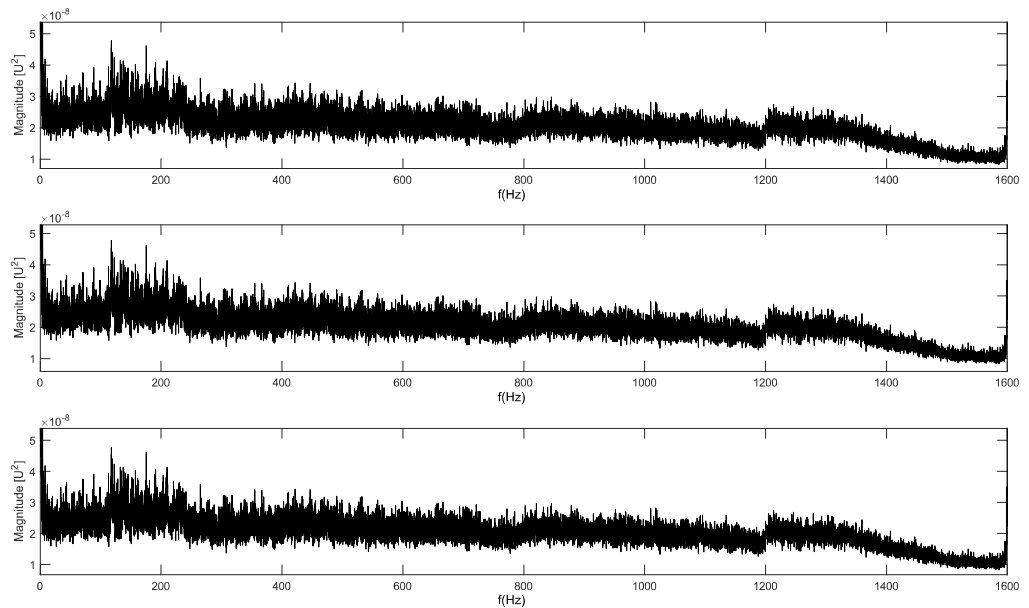


Figure 16. ES of the raw signals of Figure 14 for a) run-up b) random and c) run-down.

## 5 Conclusion

This paper aims at introducing an autonomous method for bearing diagnosis. It relies on the introduction of a new scalar indicator, which gives the probability of the presence of a fault in a given component of the bearing. The indicator results from a post-processing of the spectral coherence, as computed by the Fast-OFSC algorithm.

All factors that are likely to impede the autonomous diagnosis have been addressed; this includes the consideration of the slip phenomenon by probing the characteristic fault

frequencies into narrow bands rather than at a specific value, but also the standardization of the estimated envelope spectrum to remove bias and frequency dependence in the estimation variance. The method comes with a robust threshold, which is crucial for decision making.

The proposed method has been validated on several databases, where it has been checked to be able to systematically replace human inspection of the envelope spectrum to efficiently complete the diagnosis of bearings.

Despite the good results obtained from the application of the proposed method on signals with constant or variable speed, this method has a limitation in the case of high-speed fluctuations. This limitation is due to the fact that the Fast-OFSC fails to evidence clearly the presence of a fault in this case. As perspective to this work, the speed profile could be sliced into several speed intervals and the Fast-OFSC calculated for each of them. Future work could also consider the optimization of the selection of the different parameters of the proposed method such as the band width size, the number of the used harmonics and the statistical threshold.

### Appendix A. Proof of Eq. (19):

Let us start by expressing the comparison of  $PPF$  with the threshold  $T$  that can give a decisive conclusion,  $I \geq T$ , where  $T$  and  $PPF$  are given respectively in Eqs. (17) and (15):

$$T = \frac{\lambda_{detect} - \lambda_{1-p}}{\lambda_{detect}} \quad \text{and} \quad PPF = \frac{1}{n} \sum_{i=1}^n PFI_i.$$

Inserting the above formulas into the decision rule Eq. (18), one has

$$\frac{1}{N} \sum_i^N PFI_i \geq \frac{1}{N} \sum_i^N \frac{(m_{bi} - \lambda_{floor}) +}{m_{bi}} \quad (A.1)$$

the next step is to replace  $PFI_i$  with its value provided in Eq. (14):

$$\frac{1}{N} \sum_i^N \left( 1 - \frac{\lambda_{floor}}{m_{bi}} \right) \geq 1 - \frac{\lambda_{floor}}{\lambda_{detect}} \quad (A.2)$$

After rearranging the above inequality, we obtain the final form introduced in Eq. (19):

$$\frac{1}{N} \sum_{i=1}^N \frac{1}{m_i} \leq \frac{1}{\lambda_{detect}}.$$

### Appendix B. Table of results of section 4.1.3

Table B.1 48 kHz normal baseline data analysis results

Data Set	The proposed method				Method provided in Ref. [25]		
	BPOO	BPOI	BSO	T	BPOO	BPOI	BSO
97	0.5578	0.2887	0.4217	0.6937	65.0582	48.8305	36.7805
98	0.4030	0.3156	0.0351	0.7245	53.8356	35.5319	19.9288
99	0.5831	0.6696	0.3142	0.6756	75.7591	23.5026	17.8074

100	0.4115	0.4308	0.5880	0.6756	54.7381	62.2203	22.9488
-----	--------	--------	--------	--------	---------	---------	---------

Table B.2 12 kHz drive end bearing fault analysis results using the proposed method

Inner race faults					Ball Fault					
Data set	BPOO	BPOI	BSO	T	Data set	BPOO	BPOI	BSO	T	Cage
105	0.9484	0.9996	0.9845	0.969	118	0.9061	0.8618	0.5841	0.6957	0.476
106	0.9015	0.9993	0.9724	0.966	119	0.9345	0.9221	0.7314	0.6881	0.493
107	0.8947	0.9994	0.9675	0.965	120	0.8250	0.8078	0.7404	0.7059	0.847
108	0.8760	0.9994	0.9741	0.962	121	0.8871	0.8926	0.7324	0.636	0.676
169	0.7595	0.9877	0.7377	0.901	185	0	0	0.4996	0.4812	0.397
170	0.7975	0.9825	0.8516	0.852	186	0	0	0	0.4675	0.837
171	0.7357	0.9810	0.7577	0.852	187	0	0	0.1285	0.4243	0.893
172	0.7779	0.9860	0.5176	0.865	188	0.1178	0	0.1275	0.5064	0.922
209	0.8886	0.9982	0.9477	0.938	222	0.2962	0.8633	0.6088	0.6069	0.367
210	0.6721	0.9961	0.6875	0.939	223	0.0294	0.0294	0.3723	0.5023	0.107
211	0.7869	0.9964	0.9097	0.925	224	0.0204	0.0175	0.1672	0.3220	0.532
212	0.6684	0.9948	0.9151	0.933	225	0.0330	0.0389	0.1011	0.1427	0.263
3001	0.4648	0.6904	0.7336	0.369	3005	0	0.2705	0.3134	0.7171	0.088
3002	0.1433	0.4849	0.8409	0.433	3006	0.2831	0.1356	0.0801	0.7144	0.094
3003	0.2715	0.8351	0.5530	0.423	3007	0.7181	0.6930	0.4268	0.7105	0.355
3004	0.1315	0.2342	0.3047	0.246	3008	0.3154	0.1144	0.9306	0.6899	0.933
Outer race faults (centered)					Outer race faults (orthogonal)					
Data set	BPOO	BPOI	BSO	T	Data set	BPOO	BPOI	BSO	T	
130	0.9969	0.5193	0.5123	0.899	156	0.9902	0.7702	0.6928	0.8476	
131	0.9987	0.7606	0.7971	0.913	158	0.8763	0.8762	0.9203	0.8725	
132	0.9988	0.8713	0.6630	0.908	159	0.9963	0.8879	0.9011	0.9384	
133	0.9985	0.7272	0.7076	0.916	160	0.9935	0.7943	0.8220	0.9035	
197	0.4502	0.8111	0.3728	0.489	-	-	-	-	-	
198	0.7809	0.9255	0.7344	0.569	-	-	-	-	-	
199	0.5943	0.8422	0.4437	0.512	-	-	-	-	-	
200	0.7622	0.9463	0.7355	0.560	-	-	-	-	-	

234	0.9665	0.3202	0.4635	0.810	258	0.9965	0.9188	0.9626	0.9709
235	0.9804	0.6164	0.5840	0.828	259	0.9966	0.9219	0.9660	0.9614
236	0.9823	0.4207	0.6522	0.829	260	0.9910	0.8739	0.9263	0.9329
237	0.9873	0.4459	0.6998	0.868	261	0.996	0.953	0.975	0.961
Outer race faults (opposite)					5	4	9	0	
Data set	BPOO	BPOI	BSO	T					
144	0.9959	0.3777	0.3637	0.931					
145	0.9926	0.2520	0.3163	0.904					
146	0.9945	0.2987	0.2319	0.886					
147	0.9940	0.7034	0.5235	0.907					
246	0.9937	0.3777	0.3637	0.904					
247	0.9793	0.2520	0.3163	0.867					
248	0.9855	0.2987	0.2319	0.874					
249	0.9807	0.7034	0.5235	0.861					

Table B.3 12 kHz drive end bearing fault analysis results using the method provided in Ref. [25]

Inner-race fault				Ball Fault			
Data set	BPOO	BPOI	BSO	Data set	BPOO	BPOI	BSO
105	80.13074	154.6154	100.2518	118	262.3606	261.3103	82.2886
106	59.95864	243.0025	218.3986	119	325.5937	368.3331	128.4190
107	58.64396	238.7624	105.4183	120	332.0724	303.1483	78.3495
108	127.1694	231.9285	28.0704	121	384.1542	306.9658	116.9734
169	63.92758	122.6963	124.0035	185	183.5029	160.7559	115.2002
170	95.5765	109.465	19.92854	186	183.2837	152.7714	102.9671
171	167.9405	134.8354	74.29297	187	172.4535	143.3505	103.7485
172	65.30441	125.9451	65.72323	188	119.1233	123.4360	101.6748
209	116.503	195.0341	86.0356	222	275.0671	337.7956	147.7960
210	94.13695	189.5171	110.9834	223	251.0303	286.1039	132.0914
211	30.72399	199.0607	23.45356	224	320.6273	348.5367	162.8276
212	95.78816	178.4996	31.8321	225	277.2431	381.4757	93.4585

3001	25.40582	38.88305	23.78085	3005	164.0249	219.3683	103.5734
3002	20.88356	29.58319	21.92808	3006	188.2123	149.9673	122.3248
3003	25.75691	23.50026	21.80714	3007	234.8507	144.4594	63.3005
3004	24.73811	22.22053	22.94868	3008	146.6482	144.6468	78.8738
Outer-race faults (centred)				Outer-race faults (orthogonal)			
Data set	BPOO	BPOI	BSO	Data set	BPOO	BPOI	BSO
135	319.9929	328.7147	116.5747	156	147.8647	128.8476	26.91156
136	315.2896	186.095	171.9141	158	139.7767	96.85972	69.24428
137	376.921	219.4763	191.3679	159	255.0334	120.4593	126.4856
138	363.1219	207.1254	196.6495	160	135.5325	119.5861	48.90483
201	35.30707	22.45357	17.84789	-	-	-	-
202	44.22257	34.38921	32.01002	-	-	-	-
203	85.8417	65.8291	55.75688	-	-	-	-
204	25.8978	34.28595	25.65946	-	-	-	-
238	162.8417	65.8291	55.75688	258	120.1833	102.0976	51.75411
239	282.1088	91.51633	86.96609	259	120.7183	70.88305	78.02365
240	250.0348	84.19078	74.3066	260	119.1585	63.04126	82.42401
241	112.4019	67.7288	50.63768	261	104.3268	19.1576	30.5906
Outer race faults (opposite)							
Data set	BPOO	BPOI	BSO				
144	77.00214	27.98118	34.53967				
145	107.4983	37.72	63.25877				
146	77.73364	107.7459	48.70744				
147	98.76796	44.71517	57.28507				
246	60.39568	43.75295	28.73693				
247	52.50831	41.1433	37.33983				
248	79.40718	53.97463	34.45013				
249	81.11029	49.31261	33.4713				

## 6 References

- [1] A. K. Jalan and A. R. Mohanty, "Model based fault diagnosis of a rotor-bearing system for misalignment and unbalance under steady-state condition," *J. Sound Vib.*, 2009.
- [2] X. Liu, L. Bo, X. He, and M. Veidt, "Application of correlation matching for automatic bearing fault diagnosis," *J. Sound Vib.*, 2012.
- [3] K. A. Loparo, M. L. Adams, W. Lin, M. F. Abdel-Magied, and N. Afshari, "Fault detection and diagnosis of rotating machinery," *IEEE Trans. Ind. Electron.*, vol. 47, no. 5, pp. 1005–1014, 2000.
- [4] L. Renforth, P. S. Hamer, D. Clark, S. Goodfellow, and R. Tower, "Continuous, remote on-line partial discharge (OLPD) monitoring of HV EX/ATEX motors in the oil and gas industry," in *Petroleum and Chemical Industry Technical Conference (PCIC), 2013 Record of Conference Papers Industry Applications Society 60th Annual IEEE*, 2013, pp. 1–8.
- [5] C. Bianchini, F. Immovilli, M. Cocconcelli, R. Rubini, and A. Bellini, "Fault detection of linear bearings in brushless AC linear motors by vibration analysis," *IEEE Trans. Ind. Electron.*, vol. 58, no. 5, pp. 1684–1694, 2011.
- [6] A. K. S. Jardine, D. Lin, and D. Banjevic, "A review on machinery diagnostics and prognostics implementing condition-based maintenance," *Mechanical Systems and Signal Processing*. 2006.
- [7] N. Tandon and A. Choudhury, "A review of vibration and acoustics measurement methods for the detection of defects in rolling element bearing," *Tribol. Int.*, 1999.
- [8] V. Sharma and A. Parey, "A Review of Gear Fault Diagnosis Using Various Condition Indicators," in *Procedia Engineering*, 2016.
- [9] P. Večeř, M. Kreidl, and R. Šmíd, "Condition Indicators for Gearbox Condition Monitoring Systems," *Acta Polytech.*, 2005.
- [10] H. Ocaik and K. A. Loparo, "Estimation of the running speed and bearing defect frequencies of an induction motor from vibration data," *Mech. Syst. Signal Process.*, 2004.
- [11] Y.-C. Choi and Y.-H. Kim, "Fault detection in a ball bearing system using minimum variance cepstrum," *Meas. Sci. Technol.*, vol. 18, no. 5, p. 1433, 2007.
- [12] R. B. Randall, J. Antoni, and S. Chobsaard, "The relationship between spectral correlation and envelope analysis in the diagnostics of bearing faults and other cyclostationary machine signals," *Mech. Syst. Signal Process.*, 2001.
- [13] J. R. Stack, R. G. Harley, and T. G. Habetler, "An amplitude Modulation detector for fault diagnosis in rolling element bearings," *IEEE Trans. Ind. Electron.*, 2004.
- [14] Y. Wang, Z. He, and Y. Zi, "A demodulation method based on improved local mean decomposition and its application in rub-impact fault diagnosis," *Meas. Sci. Technol.*, 2009.
- [15] Q. Meng and L. Qu, "Rotating machinery fault diagnosis using Wigner distribution," *Mech. Syst. Signal Process.*, 1991.

- [16] A. C. McCormick and A. K. Nandi, "Cyclostationarity in rotating machine vibrations," *Mech. Syst. Signal Process.*, 1998.
- [17] I. Antoniadis and G. Glossiotis, "Cyclostationary analysis of rolling-element bearing vibration signals," *J. Sound Vib.*, vol. 248, no. 5, pp. 829–845, 2001.
- [18] W. Gardner and L. Franks, "Characterization of cyclostationary random signal processes," *IEEE Trans. Inf. theory*, vol. 21, no. 1, pp. 4–14, 1975.
- [19] G. D. Živanović and W. A. Gardner, "Degrees of cyclostationarity and their application to signal detection and estimation," *Signal Processing*, vol. 22, no. 3, pp. 287–297, 1991.
- [20] P. PRIEUR and G. D'URSO, "Des indices de cyclostationnarité pour la surveillance des engrenages," in *15<sup>o</sup> Colloque sur le traitement du signal et des images, FRA, 1995*, 1995.
- [21] A. Raad, J. Antoni, and M. Sidahmed, "Indicators of cyclostationarity: Theory and application to gear fault monitoring," *Mech. Syst. Signal Process.*, vol. 22, no. 3, pp. 574–587, 2008.
- [22] R. B. Randall and J. Antoni, "Rolling element bearing diagnostics—A tutorial," *Mech. Syst. Signal Process.*, vol. 25, no. 2, pp. 485–520, 2011.
- [23] P. Pennacchi, P. Borghesani, S. Chatterton, and R. Ricci, "An experimental based assessment of the deviation of the bearing characteristic frequencies."
- [24] W. A. Smith and R. B. Randall, "Rolling element bearing diagnostics using the Case Western Reserve University data: A benchmark study," *Mech. Syst. Signal Process.*, vol. 64, pp. 100–131, 2015.
- [25] A. Klausen, K. G. Robbersmyr, and H. R. Karimi, "Autonomous Bearing Fault Diagnosis Method based on Envelope Spectrum," *IFAC-PapersOnLine*, vol. 50, no. 1, pp. 13378–13383, 2017.
- [26] J. Antoni, G. Xin, and N. Hamzaoui, "Fast computation of the spectral correlation," *Mech. Syst. Signal Process.*, vol. 92, pp. 248–277, 2017.
- [27] A. V. Dandawate and G. B. Giannakis, "Statistical tests for presence of cyclostationarity," *IEEE Trans. signal Process.*, vol. 42, no. 9, pp. 2355–2369, 1994.
- [28] J. Antoni, "Cyclic spectral analysis of rolling-element bearing signals: Facts and fictions," *J. Sound Vib.*, vol. 304, no. 3–5, pp. 497–529, 2007.
- [29] J. Antoni, "Cyclic spectral analysis in practice," *Mech. Syst. Signal Process.*, vol. 21, no. 2, pp. 597–630, 2007.
- [30] J. Antoni and D. Hanson, "Detection of surface ships from interception of cyclostationary signature with the cyclic modulation coherence," *IEEE J. Ocean. Eng.*, vol. 37, no. 3, pp. 478–493, 2012.
- [31] "IMS bearings dataset," 2014. [Online]. Available: <http://ti.arc.nasa.gov/tech/dash/pcoe/prognosticdata->
- [32] "The Case Western Reserve University Bearing Data Center Website." [Online]. Available: <https://csegroups.case.edu/bearingdatacenter/>.
- [33] C. Mishra, A. K. Samantaray, and G. Chakraborty, "Rolling element bearing defect diagnosis under variable speed operation through angle synchronous averaging of wavelet de-noised estimate," *Mech. Syst. Signal Process.*, vol. 72, pp. 206–222, 2016.

- [34] W. Gousseau, J. Antoni, and J. Griffaton, "Analysis of the Rolling Element Bearing data set of the Center for Intelligent Maintenance Systems of the University of Cincinnati."
- [35] H. Qiu, J. Lee, J. Lin, and G. Yu, "Wavelet filter-based weak signature detection method and its application on rolling element bearing prognostics," *J. Sound Vib.*, vol. 289, no. 4–5, pp. 1066–1090, 2006.
- [36] W. Li, M. Qiu, Z. Zhu, F. Jiang, and G. Zhou, "Fault diagnosis of rolling element bearings with a spectrum searching method," *Meas. Sci. Technol.*, vol. 28, no. 9, p. 95008, 2017.
- [37] D. Abboud and J. Antoni, "Order-frequency analysis of machine signals," *Mech. Syst. Signal Process.*, vol. 87, pp. 229–258, Mar. 2017.